processes

MDPI

Article

A Preliminary Numerical Study on the Performance of Cyclone Separators in Supercritical CO_2 Solar Power Plants

Anjun Li [1], Ziang Zhu [2], Peikun Liu [1] and Xiaoyu Li [1,*]

[1] School of Mechanical and Electronic Engineering, Shandong University of Science and Technology, Qingdao 266590, China
[2] School of New Energy, China University of Petroleum (East China), Qingdao 266580, China
* Correspondence: 18561945280@163.com; Tel.: +86-185-6194-5280

Abstract: A combined approach of computational fluid dynamics, the discrete phase model, and the wall erosion model was used to numerically investigate the hydrodynamics, separation efficiency, and erosion rate in cyclone separators for s-CO_2 solar power plants. Moreover, the results were compared with those for air and CO_2 as carrier phases. The experimental data from the literature were used to validate the numerical model, and it was observed that the simulated gas velocities and wall erosion rate accurately aligned with the experimental measurements. The numerical results reveal that s-CO_2 had the largest tangential velocity compared to the other two media; its area-weighted axial velocity of upward flow was the lowest in the middle part of the cyclone body, and varied considerably in the bottom region of the conical section. The particles were all collected at the bottom surface of air and CO_2, but the separation efficiency of s-CO_2 was 81.51%, due to the poor distribution of the vortex and short circuit. Finally, the erosion rate distribution and averaged surface erosion rate were also analyzed for the three carrier phases.

Keywords: solar tower power; cyclone separator; supercritical CO_2; erosion rate; separation efficiency

check for updates

Citation: Li, A.; Zhu, Z.; Liu, P.; Li, X. A Preliminary Numerical Study on the Performance of Cyclone Separators in Supercritical CO_2 Solar Power Plants. *Processes* **2023**, *11*, 3297. https://doi.org/10.3390/pr11123297

Academic Editor: Paola Ammendola

Received: 3 November 2023
Revised: 21 November 2023
Accepted: 24 November 2023
Published: 25 November 2023

1. Introduction

Solar power tower (SPT) plants convert solar thermal energy into electricity by using concentrated solar radiation to heat the heat transfer fluid (HTF) in a solar receiver [1,2]. Thanks to the implementation of the thermal energy storage (TES) system, SPT plants are able to store and utilize energy more efficiently [3,4]. Figure 1 sketches a configuration of an SPT plant using supercritical CO_2 (T > 31.1 °C and P > 7.38 MPa) as HTF [5]. The properties of s-CO_2 fall between those of gases and liquids, providing the benefits of high diffusivity and low viscosity. As a result, it finds wide application in diverse industries such as chemical engineering, energy, pharmaceuticals, and materials science. Here, the s-CO_2 produced under high-pressure and -temperature conditions is suitable as a superb working fluid for supercritical CO_2 Brayton cycles [6]. As illustrated in Figure 1, a TES tank containing granular material is suggested for the purpose of storing surplus thermal energy generated during peak sunlight hours and utilizing it when required in the future. The TES tank is suggested to operate in a fluidized bed regime [7]. Throughout the processes of charging and discharging, particles may be carried out of the tank and flow into the turbine, due to the drag force exerted by the gas. As shown in Figure 2, stationary blades can be eroded by high-pressure steam streamlines laden with particles [8]. Hence, cyclone separators are incorporated into the s-CO_2 circulation system to safeguard the turbine against particle erosion.

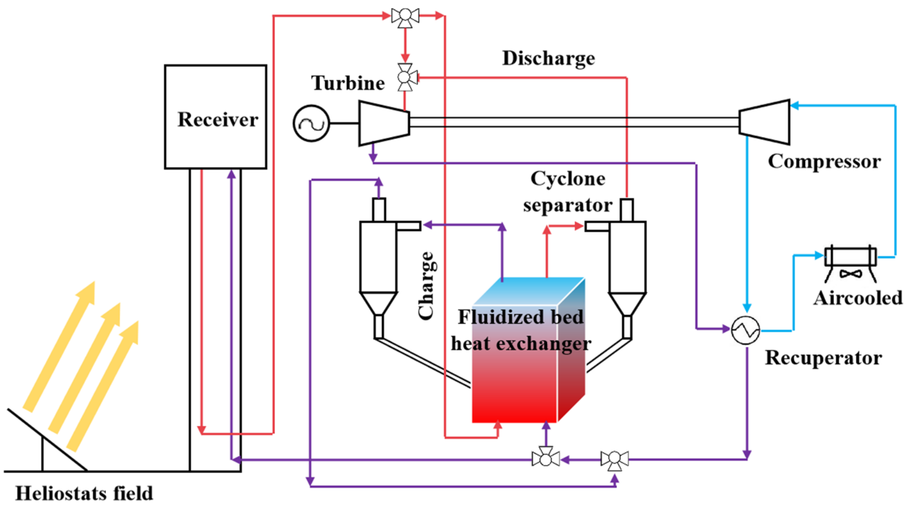

Figure 1. Sketch of solar power plant using supercritical CO_2 as working fluid.

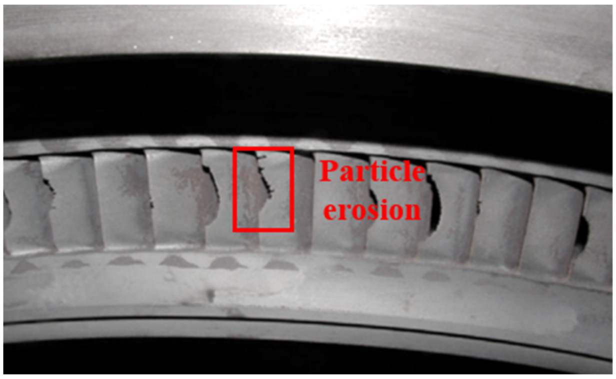

Figure 2. Particle erosion of blades in a high-pressure turbine [8].

Cyclone separators are crucially important in a variety of industrial applications because of their uncomplicated geometries and cost-efficient manufacturing and operation. The impurities will be separated from fluids under the action of centrifugal force. For air cyclone separators, numerous experimental and numerical studies have been conducted on the effects of various geometric designs and operating conditions on flow behavior, separation efficiency, and erosion rates [9–12]. For CO_2 cyclone separators, Yamasaki et al. [13] proposed a novel CO_2 dry-ice cyclone separator to separate solid-gas CO_2, where the working condition is below 0.518 MPa and −56.6 °C. Li et al. [14] used a mixture of supercritical water and s-CO_2 as the working medium and found that a significant increase in the pressure drop would occur with the rise in the content of s-CO_2 at the inlet. Tang et al. [15] improved the axial-flow cyclone to realize the separation of gas–liquid phases of supercritical CO_2 and water. It can be found that very few attempts have been focused on cyclone separators using pure s-CO_2 as the carrier phase, and it remains unclear how traditional air cyclone separators' structure and operating parameters would perform when applied to s-CO_2.

Due to the high-pressure conditions of s-CO_2, the CFD-DPM method is a highly important numerical technique used to predict the behavior of particles and flow fields within a cyclone. For instance, Li and Lu [16] applied this method to design supercritical water cyclones with different circular inlets at a pressure of 23 MPa. Li et al. [17] utilized CFD-DPM simulations to enhance the design of the axial-flow cyclone for separating water droplets from natural gas at pressures between 7.21 MPa and 7.80 MPa. In the present work, the performance of cyclones with different carrier phases was investigated using the Eulerian–Lagrangian two-phase method. Experimental data available in the literature were used to validate the numerical model. The hydrodynamics, separation efficiency, and wall erosion rate when using air and (supercritical) CO_2 as carrier phases were compared. The objective is to explore the performance of traditional air cyclone-separator dimensions and operating conditions in s-CO_2 and provide suggestions for optimization.

2. Numerical Model Description

2.1. Governing Equations of Continuous Phases

The continuous phases are determined by solving the three-dimensional Reynolds-averaged Navier–Stokes equation. The continuity and momentum equations are provided as:

$$\frac{\partial \rho}{\partial t} + \nabla \cdot (\rho \boldsymbol{u}) = 0 \tag{1}$$

$$\frac{\partial}{\partial t}(\rho \boldsymbol{u}) + \nabla \cdot (\rho \boldsymbol{u}\boldsymbol{u}) = -\nabla p + \nabla \cdot (\boldsymbol{\tau}) + \rho \boldsymbol{g} + \boldsymbol{S}_p \tag{2}$$

In Equations (1) and (2), the variable $\boldsymbol{u}$ represents gas velocity and ρ represents the density of the gas phase. The acceleration caused by gravity is denoted as $\boldsymbol{g}$. p and $\boldsymbol{\tau}$ are the static pressure and stress tensor of carrier phases, respectively [18]. $\boldsymbol{S}_p$ stands for the interaction of particles on fluids.

The Reynolds Stress Model (RSM), a widely utilized model for simulating gas cyclone separators, is employed to address turbulent flow. The transport equation of the Reynolds stress term can be written as:

$$\begin{aligned} \frac{\partial}{\partial t}\left(\rho \overline{u_i' u_j'}\right) + \frac{\partial}{\partial x_k}\left(\rho u_k \overline{u_i' u_j'}\right) = & -\frac{\partial}{\partial x_k}\left[\frac{\mu_t}{\sigma_k}\frac{\partial \overline{u_i' u_j'}}{\partial x_k}\right] + \frac{\partial}{\partial x_k}\left[\mu \frac{\partial}{\partial x_k}\left(\overline{u_i' u_j'}\right)\right] \\ & -\frac{\mu_t}{\rho Pr_t}\left(g_i \frac{\partial \rho}{\partial x_j} + g_j \frac{\partial \rho}{\partial x_i}\right) + p'\left(\frac{\partial u_i'}{\partial x_j} + \frac{\partial u_j'}{\partial x_i}\right) - \frac{2}{3}\delta_{ij}(\rho \varepsilon + Y_M) \end{aligned} \tag{3}$$

where subscripts i, j, and k are coordinates. On the right side of Equation (3), five terms refer to turbulent diffusion ($D_{T,ij}$), molecular diffusion ($D_{L,ij}$), buoyancy production (G_{ij}), pressure strain (Φ_{ij}), and dissipation (ε_{ij}), respectively. Φ_{ij} is modeled using the linear pressure–strain model [19].

2.2. Dispersed-Phase Equations

Solids are tracked in the Lagrangian framework, whereby their motion is calculated using Newton's second law. The expression for the linear momentum of a particle is given by:

$$\frac{d\boldsymbol{u}_p}{dt} = \frac{18\mu}{\rho_p d_p^2}\frac{C_D Re_p}{24}(\boldsymbol{u} - \boldsymbol{u}_p) + \frac{\rho_p - \rho}{\rho_p}\boldsymbol{g} + \frac{\rho}{\rho_p}\boldsymbol{u}_p \nabla \boldsymbol{u} \tag{4}$$

where $\boldsymbol{u}_p$ represents the velocity of the discrete phase and ρ_p refers to the particle density. μ stands for the molecular viscosity of the continuous phases, and d_p denotes the particle diameter. The particle acceleration (force per unit particle mass) is acted upon by three forces on the right side of Equation (4): drag, buoyancy, and pressure gradient. Moreover, the drag coefficient is represented by C_D:

$$C_D = a_1 + \frac{a_2}{Re_p} + \frac{a_3}{Re_p} \tag{5}$$

The constant coefficients of smooth spherical particles, namely a_1, a_2, and a_3, are determined by the Reynolds number [20]. Re_p is given by:

$$Re_p = \frac{\rho d_p \left|\boldsymbol{u}_p - \boldsymbol{u}\right|}{\mu} \tag{6}$$

The turbulence might influence the dispersion of particles. Therefore, a particle–eddy interaction model [21] was employed to illustrate how the turbulent velocity fluctuations at that moment affect the trajectory of particles. It is assumed that the turbulent pulsation velocity conforms to a Gaussian probability distribution and can be represented as:

$$u' = \zeta\sqrt{\overline{u'^2}} \tag{7}$$

In Equation (7), ζ represents a normally distributed random number. u' stands for the fluctuation velocity.

2.3. Erosion Modeling

Erosion on the wall surface results from particle impacts, and depends on particle velocities and angles. In the present work, an erosion model [22], which adopts Finnie's [23] formulation, was used to describe discrete particles abrading the cyclone surface. As illustrated in Equations (8) and (9), ER represents the erosion rate, n denotes the power-law exponent of the particle impact velocity, and K stands for the scaling parameter. The expression of Chen et al. [24] was used to describe the incidence-angle effect on surface erosion. The values for K, n, and other parameters are listed in Table 1.

$$ER = Ku_p^n f(\theta) \tag{8}$$

$$f(\theta) = \begin{cases} B\theta^2 + C\theta^2 & \text{for } \theta \leq 23^\circ \\ X\cos^2\theta\sin(W\theta) + Y\sin^2\theta + Z & \text{for } \theta > 23^\circ \end{cases} \tag{9}$$

Table 1. Erosion model empirical constants [22].

Parameter	Value
B	-7
C	5.45
X	0.4
Y	-0.9
Z	1.556056
W	-3.4
n	2.2
K	1.44×10^{-8}

2.4. Computational Geometry

The geometric model of the cyclone separator is demonstrated in Figure 3a, with specific dimensions provided in Table 2. The center of the top cover served as the reference point for the coordinates, and the direction of gravity was oriented along the negative y-axis. GAMBIT 2.4.6 software, developed by ANSYS Inc. in Canonsburg, PA, USA, was used to generate structured hexahedron grids for the computational domain of the cyclone separator (see Figure 3b). The grid independence verification is discussed in Section 2.6.

Table 2. Structural parameters of cyclone separator.

Parameter	Value	Parameter	Value
D (mm)	290	D_c/D	0.37
a/D	0.5	H/D	4.0
b/D	0.2	h_e/D	0.5
D_e/D	0.5	h_c/D	2.5

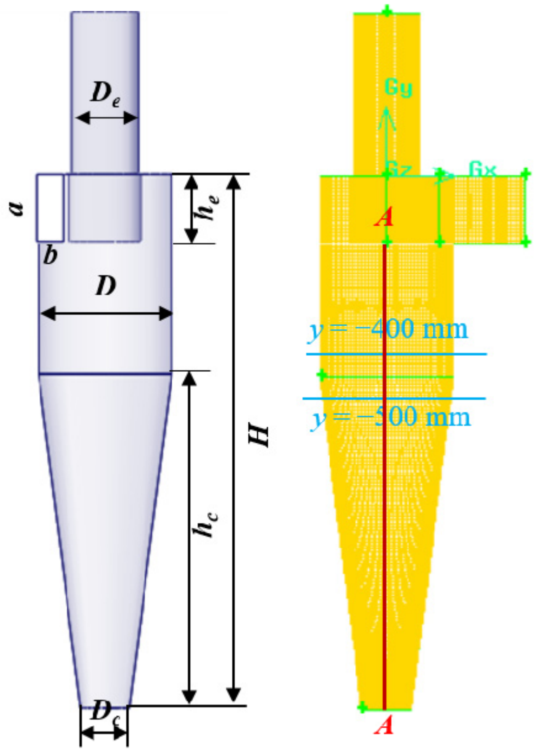

(**a**) geometric model (**b**) grid division

Figure 3. Geometrical modeling and mesh division.

2.5. Boundary Conditions and Numerical Schemes

The physical properties of air, CO_2, and s-CO_2 are listed in Table 3. Their densities are calculated using the incompressible ideal gas law, provided as:

$$\rho = p/(\frac{R}{M_w}T) \tag{10}$$

Table 3. Parameters used in the simulations.

Media	Density (kg/m^3)	Viscosity (Pa·s)	Temperature (K)	Pressure (MPa)
air	Ideal gas law	1.82×10^{-5}	293	0.1
CO_2	Ideal gas law	1.47×10^{-5}	293	0.1
s-CO_2	Ideal gas law	4.12×10^{-5}	973	15

The operating temperature and pressure are represented by T and p, respectively, while the molecular weight of the carrier phase is denoted by M_w, and R signifies the universal gas constant.

The discrete particles were considered to be spherical sand solids with a density of 2650 kg/m^3 and a diameter of 10 μm. The inlet mass flow rate of the particles is 0.001354 kg/s. As reported in the literature [25,26], the inlet velocity of cyclone separators ranges from 10 m/s to 30 m/s. Hence, for this work, a gas velocity of 16.1 m/s was specified at the tangential inlet. The "pressure-outlet" boundary condition was utilized at the end of the exhaust pipe. Sand particles are trapped when they move to the bottom and escape through the exhaust pipe. The standard wall functions were utilized to describe the alterations in momentum in the near-wall zone. A "no-slip" boundary condition was applied to the wall for the continuous phases, and the momentum of particles would be reduced after colliding with the wall. The reduction in kinetic energy can be expressed as elucidated by the restitution model developed by Grant and Tabakoff [27], which can be expressed as:

$$e_n = 0.993 - 1.76\theta + 1.56\theta^2 - 0.49\theta^3 \quad (11)$$

$$e_t = 0.998 - 1.55\theta + 2.11\theta^2 - 0.67\theta^3 \quad (12)$$

where θ is the impact angle of the particles. e_n and e_t are the normal and tangential coefficients.

The CFD-DPM method was employed in ANSYS FLUENT 19.2, which utilizes the finite volume method in structured meshes to solve the gas-phase equations mentioned above and tracks particles in the domain using Lagrangian coordinates [28,29]. All the simulations were carried out in parallel on a workstation with a 48 $\times$ 2.8 GHz processor and 256 GB RAM. The continuous phase and discrete particles mutually influenced each other's motion, through drag force. For pressure–velocity coupling, the SIMPLEC algorithm was employed. A second-order scheme was utilized to discretize the convective and divergence terms, while the pressure interpolation was performed using the PRESTO! discretization scheme. The convergence criterion accuracy was set to 1×10^{-4}. A time-step size of 1×10^{-4} s and 20 interactions per time-step were used in the simulations.

2.6. Grid Independence Study

Mesh independence was performed to achieve a balance between computational cost and the quality of results, where four different grid strategies were selected. The simulations of the single-phase flow of air were calculated. Figure 4 depicts the radial distribution of gas magnitude velocity at $y = -400$ mm and the pressure drop between the entrance and outlet, respectively. As shown in Figure 4a, the tangential velocities of grid numbers of ~0.58 million and ~1.14 million were relatively consistent. From Figure 4b, it can be observed that the pressure drop had a maximum error of 1.77% when the number of grids exceeded 0.29 million. Consequently, the remaining simulations were carried out on a medium-sized grid of ~0.58 million.

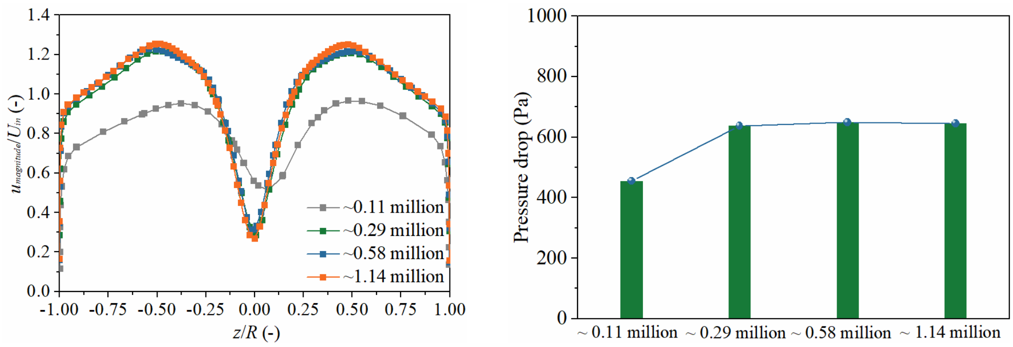

(**a**) magnitude velocity (**b**) pressure drop

Figure 4. Distribution of magnitude velocity and pressure drop under different grid strategies.

3. Results and Discussion

3.1. Model Validation

To confirm the reasonableness of the hydrodynamics and erosion rate estimated by the current numerical model, simulations were carried out in this subsection using the experimental arrangements of Hoekstra [30] and Solnordal et al. [22]. Figure 5 shows the comparison of mean tangential and axial velocities of the gas phase at axial location $|y/D| = 0.75$ between simulation and experiment, and Figure 6 illustrates the calculated erosion rate on the 90°-bend wall compared with the experimental results. The numerical results obtained from the present flow and erosion models fall within an acceptable range and show good agreement with the experimental data, indicating the reliability of the current findings for further analysis.

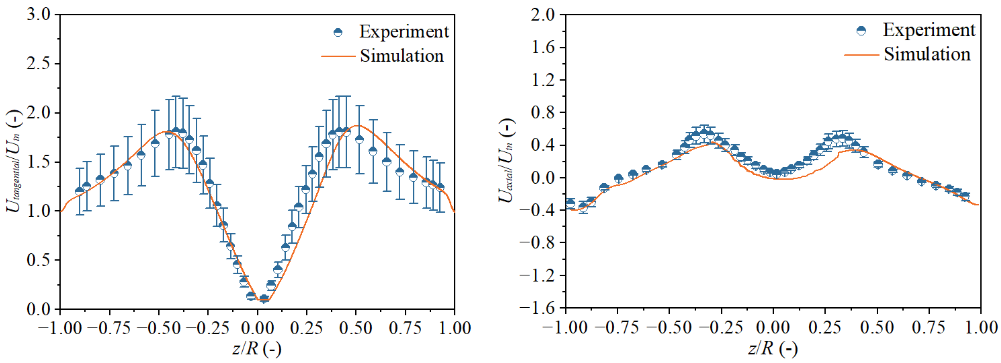

(**a**) tangential velocity (**b**) axial velocity

Figure 5. Validation of numerical simulations with experimental data at $|y/D|$ = 0.75 [30].

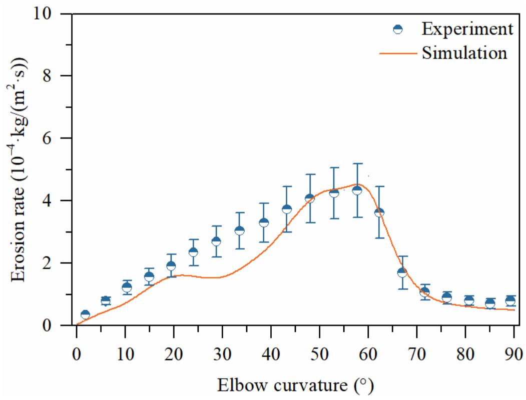

Figure 6. Comparison of the erosion rate between numerical and experimental results [22].

3.2. Hydrodynamics

Gas movement within a cyclone separator predominantly results from the tangential velocity, inducing particle migration towards the sidewall, due to centrifugal acceleration. This phenomenon significantly influences separation efficiency [14,31]. Figure 7 displays the contour plots of tangential velocity at x = 0 mm under different carrier phases. The presented tangential velocity distributions showcased the characteristic formations of the Rankine vortex model, which encompassed both the Inner Quasi-Forced Vortex (IQFV) and the Outer Quasi-Free Vortex (OQFV). In IQFV, the gas exhibited nearly rigid-body rotation, characterized by radial growth in tangential velocity. In OQFV, tangential velocity exhibited a decline along the radial direction. It can also be noted that the dividing point of IQFV and OQFV was in the bottom region of the exhaust pipe. For different carrier phases, the largest peak tangential velocity of the Rankine vortex occurred with the utilization of s-CO_2. Figure 8 shows radial profiles of tangential velocity at different heights. The curves were M–shaped and symmetrical with respect to the y-axis, which is consistent with the results in the literature [32–35]. For different carrier phases, the maximum tangential velocity of s-CO_2 in both cross-sections was ~1.82 times the inlet velocity, while the other two conventional media were ~1.07 times (air) and ~1.23 times (CO_2), respectively. Moreover, the radius position of the maximum tangential velocity (r_{max}) of air, CO_2, and s-CO_2 were ~0.56, ~0.49, and ~0.43, respectively. From the literature [36], the tangential velocity in IQFV and OQFV can be respectively written as:

$$u_{t,\mathrm{IQFV}}(r) = \Omega_0 \times r \tag{13}$$

$$u_{t,\mathrm{OQFV}}(r) \times r = \Gamma = K_0 \times u_{in} \times (\frac{D}{2} - \frac{D_{in}}{2}) \tag{14}$$

where Ω_0 represents the angular velocity, r is the radial distance, Γ denotes the circulation of OQFV, K_0 is a constant value that increases with the Reynolds number, D is the diameter of the cyclone body, and D_{in} is the hydraulic diameter of the inlet. The correlation between Γ and Ω_0 can be determined by r_{max}, which is given by:

$$r^2_{\max} \times \Omega_0 = \Gamma \tag{15}$$

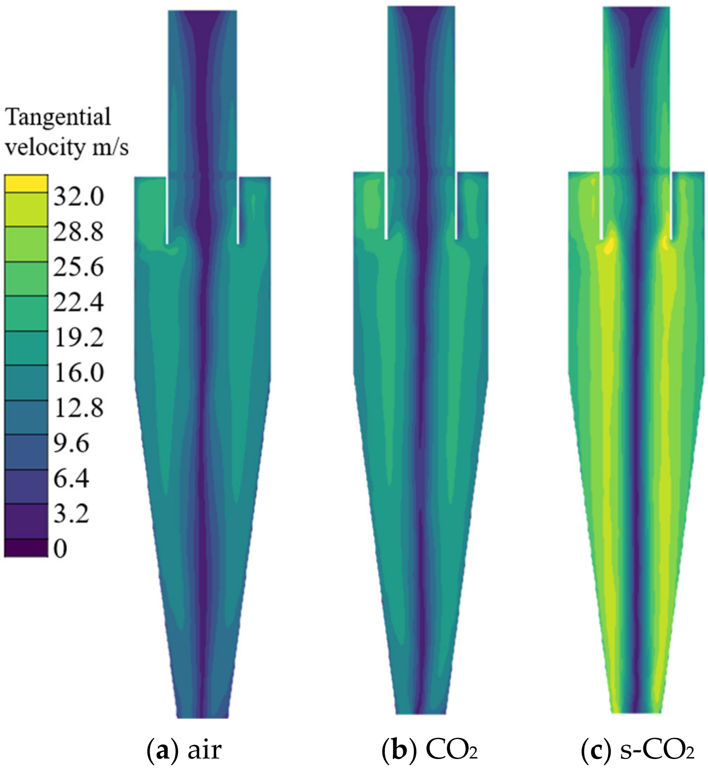

Figure 7. Distributions of tangential velocity at x = 0 mm.

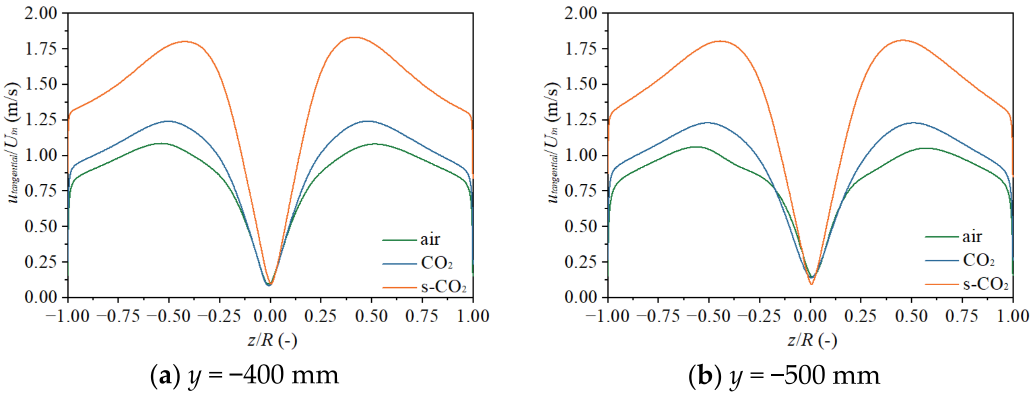

Figure 8. Radial profiles of tangential velocity at different heights.

From the above equations, s-CO_2 had a higher Reynolds number and then a larger K_0, due to its small kinematic viscosity ($v = \mu/\rho$), than other media, leading to the increase in tangential velocity.

The axial movement of particles within the cyclone body is dictated by the prominent influence exerted by the gas phase's axial velocity. Ultimately, this determines whether the particles will be collected at the bottom or escape from the outlet [37]. Figures 9 and 10 illustrate the contours and radial profiles of axial velocity under different carrier phases, respectively. It can be observed that axial velocity distributions at x = 0 mm of s-CO_2

and CO_2 were asymmetrical with the geometric axis of the cyclone separator, while the distribution of air was symmetrical. In addition, the axial velocities of air and CO_2 contained two main regions, i.e., the positive velocity at the center and the negative velocity near the sidewall. A positive axial velocity indicates an upward motion of the carrier phase, whereas a negative axial velocity implies downward movement of the fluid. However, a negative axial velocity appeared in the central region of s-CO_2, indicating the disruption of upstream flow, thus reducing the separation efficiency. Figure 11 depicts the Zero Axial Velocity Envelope (ZAVE) of cyclones with different carrier phases. The ZAVE showed a slight distortion, as the flow was unstable under the one-side inlet. For the carrier phase of s-CO_2, the shape of ZAVE was wider, and the surface at the bottom region was not enclosed.

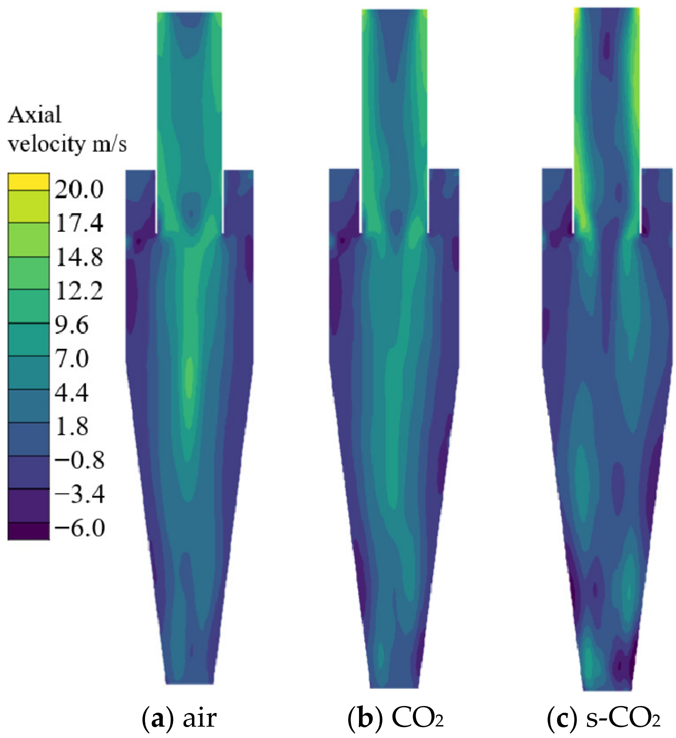

Figure 9. Distributions of axial velocity at x = 0 mm.

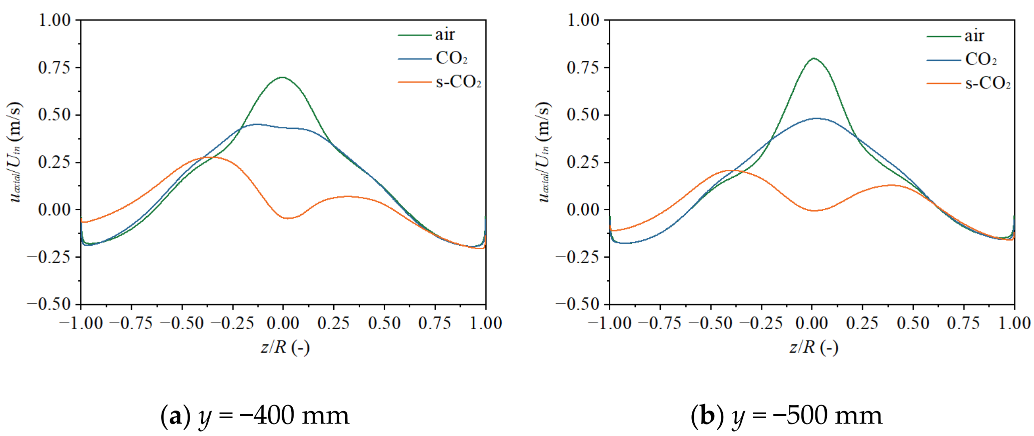

Figure 10. Radial profiles of axial velocity at different heights.

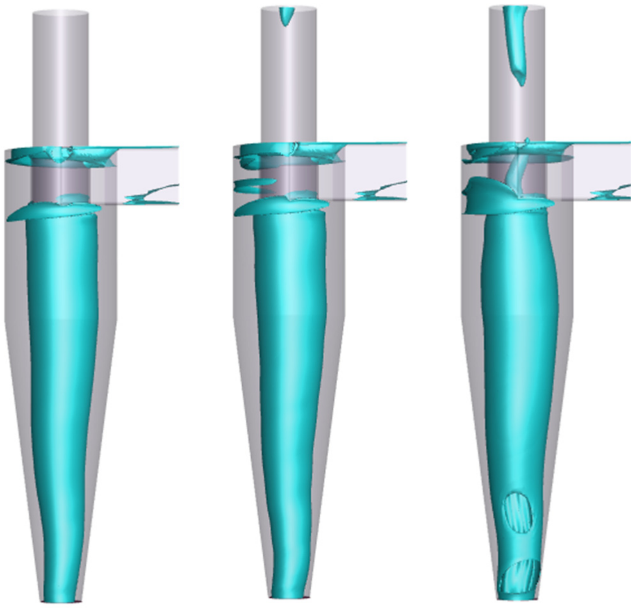

Figure 11. Enveloping surfaces of the zero axial velocity of cyclones with different carrier phases.

Figure 12 shows the streamlines on section x = 0 mm under different carrier phases. Vortex structures were visible in the cylindrical section and the conical section, as well as in the bottom region of the top cover for various carrier phases. For air and CO_2, the vortex was flattened along the axial direction, which had a minimal impact on the upstream flow. However, in the case of s-CO_2, the vortex extended in the radial direction, disrupting the upstream flow. This led to the enclosed surface of ZAVE.

$$\overline{u}_{axial,UF} = \frac{\sum_{i}^{n} u_{axial,UF,i} a_i}{\sum_{i=1}^{n} a_i} \tag{16}$$

$$I_{aixal} = \left(\frac{\sum_{i}^{n} u_{axial,UF,i} a_i}{\sum_{i=1}^{n} a_i}\right) \cdot \left(\frac{\sum_{i}^{n} u_{axial,UF,i} a_i}{\sum_{i=1}^{n} a_i} + \left|\frac{\sum_{j}^{m} u_{axial,DF,j} a_j}{\sum_{j=1}^{m} a_j}\right|\right)^{-1} \tag{17}$$

To quantitatively characterize the variations in the upward flow of different carrier phases, the area-weighted axial velocity ($\overline{u}_{axial,UF}$) and intensity (I_{axial}) of upward flow on different cross-sections were obtained, respectively. In Equations (16) and (17), $u_{axial,UF,i}$ and $u_{axial,DF,j}$ are the axial velocity of upward flow and downward flow in i_{th} and j_{th} grid on a specific cross-section, and a_i and a_j are the corresponding grid area, respectively. As illustrated in Figure 13a, $\overline{u}_{axial,UF}$ of air and CO_2 increased with the y-axis. In the case of s-CO_2, $\overline{u}_{axial,UF}$ was lower in the middle part (-700 mm < y < -400 mm) of the cyclone, and varied considerably in the bottom region of the conical section. Moreover, from Figure 13b, it can be seen that, compared with air and CO_2, I_{axial} of s-CO_2 was the lowest.

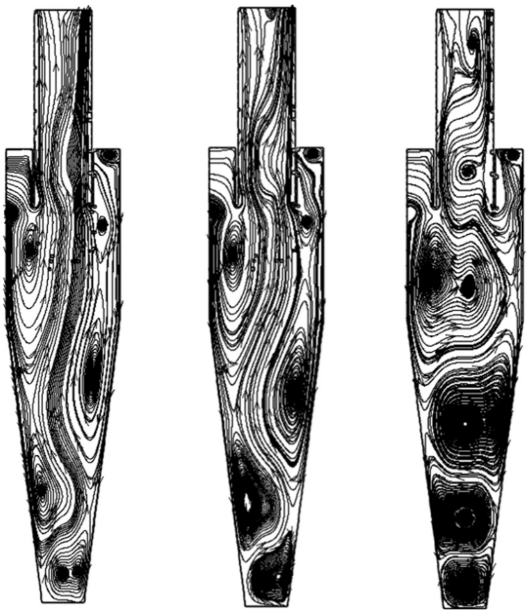

Figure 12. Streamlines on section x = 0 mm under different carrier phases.

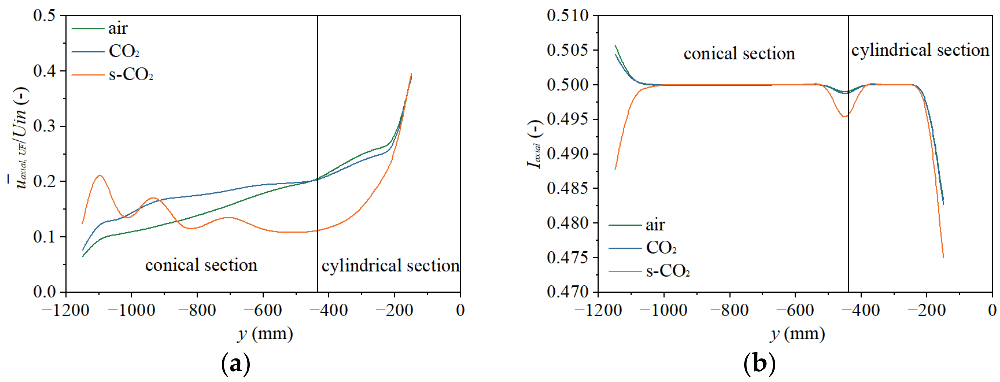

Figure 13. Area-weighted axial velocity and intensity of upward flow. (**a**) area-weighted axial velocity of upward flow (**b**) intensity of upward flow.

3.3. Separation Efficiency

The study of cyclone efficiency is highly important because cyclone separators are commonly used gas–solid separation equipment in various carrier phases. The cyclone efficiency for particles of a given diameter is given by:

$$\eta = (1 - \frac{m_{p,out}}{m_{p,in}}) \times 100\% \tag{18}$$

In the above equation, $m_{p,out}$ and $m_{p,in}$ are the mass flow rate of particles leaving through the exhaust pipe and entering the cyclone separator, respectively. Table 4 presents the separation efficiency of particles with a diameter of 10 µm in cyclone separators with different carrier phases. The particles were all collected at the bottom surface of air and CO_2, while the separation efficiency of s-CO_2 was 81.51%. For conventional media such as air, particles with a diameter above 5 µm can be effectively captured [38]. The inefficiency of the separation of s-CO_2 is due to the poor distribution of the vortex, as illustrated in Figure 12c. The particles that reached the walls would be carried back to the central region and would escape with the upstream flow. Figure 14 shows the particle paths inside the cyclone separator under different carrier phases. The particle flow in s-CO_2 was unable to maintain a good spiral shape in the column section. Some particles can also escape from the exhaust pipe through a short circuit to reduce the separation efficiency. Hence, to enhance the separation efficiency of s-CO_2, it is necessary to address the short-circuit issue and improve the distribution of vortices.

Table 4. Separation efficiency of different carrier phases.

Media	Air	CO_2	s-CO_2
η	100%	100%	81.51%

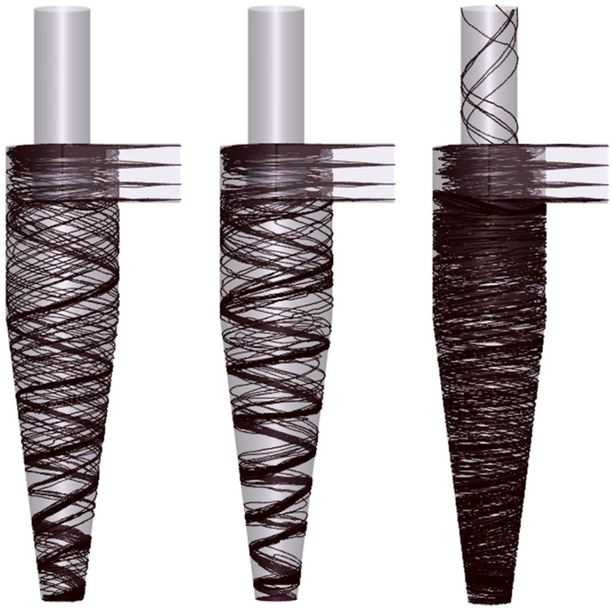

(**a**) air (**b**) CO_2 (**c**) s-CO_2

Figure 14. Particle paths inside the cyclone separator under different carrier phases.

3.4. Erosion

Figure 15 demonstrates the contour of erosion rate on the wall for various carrier phases. It can be observed that the overall erosion-wear zone of the cyclone separator followed spiral trajectories, and the erosion spiral bands had a certain width. As the axial height of the cyclone increased, the spacing between the spiral bands decreased. Moreover, the spiral erosion-wear pattern became more prominent at lower heights.

$$ER_{ave} = \sum_{k=1}^{l} \frac{ER_k a_k}{A} \tag{19}$$

For the carrier phase of s-CO_2, the erosion peak at the end of the cone was caused by the high velocity of OQFV and the movement of the vortex. The particles would be drawn into the vortex and impact this area with high speed for a prolonged period. In addition, erosion was observed on the exhaust wall surface, due to the impact of particles that had escaped. The averaged surface erosion rate ER_{ave}, given by Equation (19), was 3.69×10^{-7}, 8.15×10^{-7}, and 7.09×10^{-6} kg/(m^2·s) for air, CO_2, and s-CO_2, respectively. In Equation (19), A is the total surface area of the cyclone; a_k and ER_k are the surface area and wall erosion rate of each wall grid, respectively. Figure 16 shows the erosion rate at line A-A (as shown in Figure 3b) on the surface of cyclone separators with different carrier phases. In the case of s-CO_2, the erosion rate was an order of magnitude higher than the other two media, and the rate of erosion increased significantly with the increasing height of the cyclone separator.

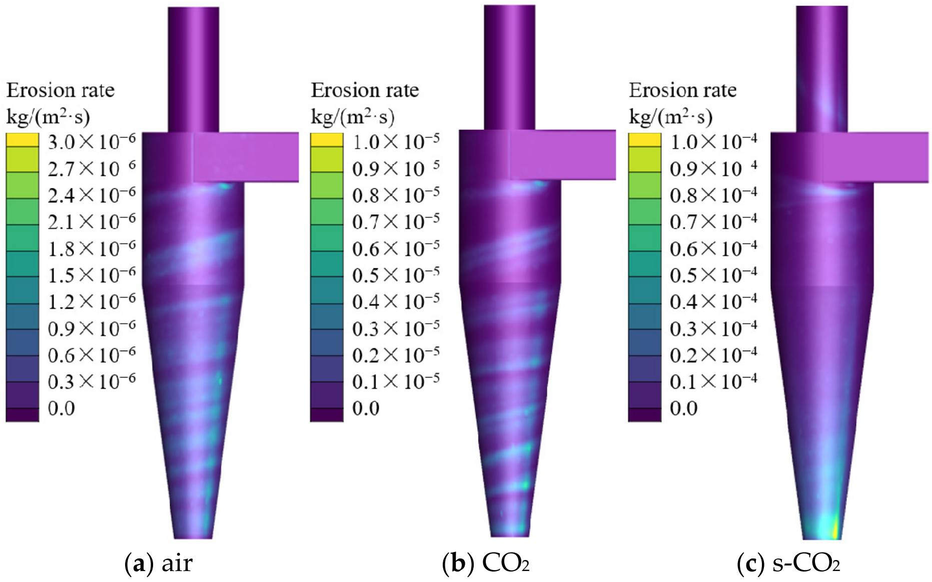

Figure 15. Contour of erosion rate on the wall for different carrier phases.

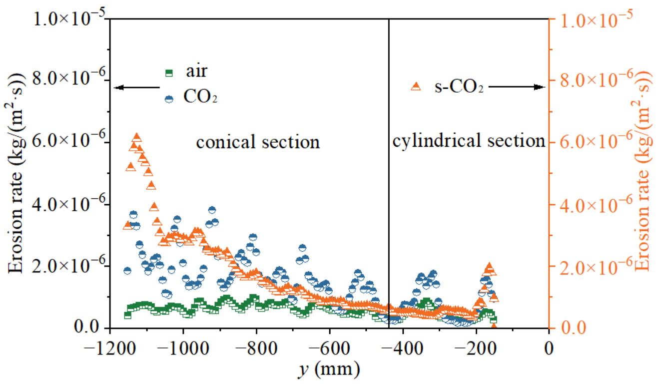

Figure 16. Erosion rate at line *A-A* on the surface of cyclone separators with different carrier phases.

4. Conclusions

In the present work, a preliminary investigation comparing the hydrodynamics, separation efficiency, and erosion rate in cyclone separators with different carrier phases (air, CO_2, and s-CO_2) was introduced, using the CFD-DPM method. The main goal is to explore the performance of traditional air cyclone-separator dimensions and operating conditions in s-CO_2.

(1) The tangential velocity distributions of various carrier phases demonstrated exemplary Rankine vortex structures. Nevertheless, among the different media, s-CO_2 exhibited a higher Reynolds number and consequently a larger K_0. This was attributed to its low kinematic viscosity, resulting in an elevated tangential velocity. The axial velocities of air and CO_2 contained two main regions, i.e., the positive velocity at the center and the negative velocity near the sidewall, while a negative axial velocity appeared in the central region of s-CO_2, indicating the disruption of upstream flow.

(2) For the carrier phase of s-CO_2, the shape of ZAVE was wider, and the surface at the bottom region was not enclosed, as a result of the vortex extending in the radial direction. In the case of s-CO_2, $\overline{u}_{axial,UF}$ was lower in the middle part of the cyclone body, and varied considerably in the bottom region of the conical section; I_{axial} was the lowest.

(3) The particles were all collected at the bottom surface of air and CO_2, while the separation efficiency of s-CO_2 was 81.51%. The inefficiency of the separation of s-CO_2 is due to the poor distribution of the vortex and short circuit. Hence, to improve the

separation efficiency of s-CO_2, the vortex distribution needs to be improved and the short-circuit problem needs to be solved.

(4) The overall erosion-wear zone of the cyclone separator with various carrier phases followed spiral trajectories, and the erosion spiral bands had a certain width. In the case of s-CO_2, the erosion rate was an order of magnitude higher than in the other two media, and the rate of erosion increased significantly with the increasing height of the cyclone separator. The erosion peak at the end of the cone was caused by the high velocity of OQFV and the movement of the vortex.

Author Contributions: Methodology, A.L.; Software, A.L.; Validation, A.L.; Writing—original draft, A.L.; Writing—review & editing, Z.Z.; Supervision, X.L.; Funding acquisition, P.L. All authors have read and agreed to the published version of the manuscript.

Funding: This work was supported by National Key Research and Development Program (No. 2023YFC2907702).

Data Availability Statement: Data sharing is not applicable.

Conflicts of Interest: The authors declare no conflict of interest.

References

1. Awan, A.B.; Mouli, K.V.V.C.; Zubair, M. Performance enhancement of solar tower power plant: A multi-objective optimization approach. *Energy Convers. Manag.* **2020**, *225*, 113378. [CrossRef]
2. Benoit, H.; Ansart, R.; Neau, H.; Triñanes, P.G.; Flamant, G.; Simonin, O. Three-dimensional numerical simulation of upflow bubbling fluidized bed in opaque tube under high flux solar heating. *AIChE J.* **2018**, *64*, 3857–3867. [CrossRef]
3. El Alami, K.; Asbik, M.; Agalit, H. Identification of natural rocks as storage materials in thermal energy storage (TES) system of concentrated solar power (CSP) plants—A review. *Sol. Energy Mater. Sol. Cells* **2020**, *217*, 110599. [CrossRef]
4. Elfeky, K.E.; Li, X.; Ahmed, N.; Lu, L.; Wang, Q. Optimization of thermal performance in thermocline tank thermal energy storage system with the multilayered PCM(s) for CSP tower plants. *Appl. Energy* **2019**, *243*, 175–190. [CrossRef]
5. Hernández-Jiménez, F.; Soria-Verdugo, A.; Acosta-Iborra, A.; Santana, D. Exergy recovery from solar heated particles to supercritical CO_2. *Appl. Therm. Eng.* **2019**, *146*, 469–481. [CrossRef]
6. Adams, B.M.; Kuehn, T.H.; Bielicki, J.M.; Randolph, J.B.; Saar, M.O. A comparison of electric power output of CO_2 Plume Geothermal (CPG) and brine geothermal systems for varying reservoir conditions. *Appl. Energy* **2015**, *140*, 365–377. [CrossRef]
7. Li, A.; Jiménez, F.; Pleite, E.; Wang, Z.; Zhu, L. Numerical comparison of thermal energy performance between spouted, fluidized and fixed beds using supercritical CO_2 as fluidizing agent. *Case Stud. Therm. Eng.* **2022**, *39*, 102469. [CrossRef]
8. Nomoto, H. 10—Solid particle erosion analysis and protection design for steam turbines. In *Advances in Steam Turbines for Modern Power Plants*; Tanuma, T., Ed.; Woodhead Publishing: Sawston, UK, 2017; pp. 219–239. [CrossRef]
9. Lim, J.-H.; Park, S.-I.; Lee, H.-J.; Zahir, M.Z.; Yook, S.-J. Performance evaluation of a tangential cyclone separator with additional inlets on the cone section. *Powder Technol.* **2020**, *359*, 118–125. [CrossRef]
10. Parvaz, F.; Hosseini, S.H.; Elsayed, K.; Ahmadi, G. Numerical investigation of effects of inner cone on flow field, performance and erosion rate of cyclone separators. *Sep. Purif. Technol.* **2018**, *201*, 223–237. [CrossRef]
11. Caliskan, M.E.; Karagoz, I.; Avci, A.; Surmen, A. An experimental investigation into the particle classification capability of a novel cyclone separator. *Sep. Purif. Technol.* **2019**, *209*, 908–913. [CrossRef]
12. Huang, A.-N.; Ito, K.; Fukasawa, T.; Fukui, K.; Kuo, H.-P. Effects of particle mass loading on the hydrodynamics and separation efficiency of a cyclone separator. *J. Taiwan Inst. Chem. Eng.* **2018**, *90*, 61–67. [CrossRef]
13. Yamasaki, H.; Kizilkan, Ö.; Yamaguchi, H.; Kamimura, T.; Hattori, K.; Nekså, P. Experimental investigation of dry ice cyclone separator for ultra-low temperature energy storage using carbon dioxide. *Energy Storage* **2020**, *2*, e149. [CrossRef]
14. Li, Z.; Tong, Z.; Yu, A.; Miao, H.; Chu, K.; Zhang, H.; Guo, G.; Chen, J. Numerical investigation of separation efficiency of the cyclone with supercritical fluid–solid flow. *Particuology* **2022**, *62*, 36–46. [CrossRef]
15. Tang, Y.; Qiao, Z.; Cao, Y.; Si, F.; Romero, C.E.; Rubio-Maya, C. Numerical analysis of separation performance of an axial-flow cyclone for supercritical CO_2-water separation in CO_2 plume geothermal systems. *Sep. Purif. Technol.* **2020**, *248*, 116999. [CrossRef]
16. Li, G.; Lu, Y. Cyclone separation in a supercritical water circulating fluidized bed reactor for coal/biomass gasification: Structural design and numerical analysis. *Particuology* **2018**, *39*, 55–67. [CrossRef]
17. Li, Y.; Qin, G.; Xiong, Z.; Fan, L. Gas-liquid separation performance of a micro axial flow cyclone separator. *Chem. Eng. Sci.* **2022**, *249*, 117234. [CrossRef]
18. Wang, T.; He, Y.; Yan, S.; Kim, D.R. Rotation characteristic and granular temperature analysis in a bubbling fluidized bed of binary particles. *Particuology* **2015**, *18*, 76–88. [CrossRef]

19. Pandey, S.; Brar, L.S. On the performance of cyclone separators with different shapes of the conical section using CFD. *Powder Technol.* **2022**, *407*, 117629. [CrossRef]
20. Morsi, S.A.; Alexander, A.J. Investigation of particle trajectories in 2-phase flow systems. *J. Fluid Mech.* **1972**, *55*, 193–208. [CrossRef]
21. Gosman, A.D.; Ioannides, E. Aspects of computer simulation of liquid-fuelled combustors. *J. Energy* **1983**, *7*, 482–490. [CrossRef]
22. Solnordal, C.; Wong, C.; Boulanger, J. An experimental and numerical analysis of erosion caused by sand pneumatically conveyed through a standard pipe elbow. *Wear* **2015**, *336–337*, 43–57. [CrossRef]
23. Finnie, I. Erosion of surfaces by solid particles. *Wear* **1960**, *3*, 87–103. [CrossRef]
24. Chen, X.; McLaury, B.; Shirazi, S. Application and experimental validation of a computational fluid dynamics (CFD)-based erosion prediction model in elbows and plugged tees. *Comput. Fluids.* **2004**, *33*, 1251–1272. [CrossRef]
25. Dehdarinejad, E.; Bayareh, M. An Overview of Numerical Simulations on Gas-Solid Cyclone Separators with Tangential Inlet. *ChemBioEng Rev.* **2021**, *8*, 375–391. [CrossRef]
26. Fu, S.; Zhou, F.; Sun, G.; Yuan, H.; Zhu, J. Performance evaluation of industrial large-scale cyclone separator with novel vortex finder. *Adv. Powder Technol.* **2021**, *32*, 931–939. [CrossRef]
27. Grant, G.; Tabakoff, W. Erosion Prediction in Turbomachinery Resulting from Environmental Solid Particles. *J. Aircr.* **1975**, *12*, 471–478. [CrossRef]
28. Wang, S.; Rao, Y.; Hao, C.; Yao, J.; Zhou, S. Numerical Simulation Study on the Influence of Twist Tape Parameters on Hydrate Particle Deposition. *Processes* **2023**, *11*, 1658. [CrossRef]
29. Brazhenko, V.; Qiu, Y.; Mochalin, I.; Zhu, G.; Cai, J.-C.; Wang, D. Study of hydraulic oil filtration process from solid admixtures using rotating perforated cylinder. *J. Taiwan Inst. Chem. Eng.* **2022**, *141*, 104578. [CrossRef]
30. Hoekstra, A.J. Gas Flow Field and Collection Efficiency of Cyclone Separators. Ph.D. Thesis, Delft University of Technology, Delft, The Netherlands, 2000.
31. Wu, J.; Zhang, Y.; Wang, H. Numerical study on tangential velocity indicator of free vortex in the cyclone. *Sep. Purif. Technol.* **2014**, *132*, 541–551. [CrossRef]
32. Li, W.; Huang, Z.; Li, G.; Ye, C. Effects of different cylinder roof structures on the vortex of cyclone separators. *Sep. Purif. Technol.* **2022**, *296*, 121370. [CrossRef]
33. Wei, Q.; Sun, G.; Gao, C. Numerical analysis of axial gas flow in cyclone separators with different vortex finder diameters and inlet dimensions. *Powder Technol.* **2020**, *369*, 321–333. [CrossRef]
34. Wang, S.; Li, H.; Wang, R.; Wang, X.; Tian, R.; Sun, Q. Effect of the inlet angle on the performance of a cyclone separator using CFD-DEM. *Adv. Powder Technol.* **2019**, *30*, 227–239. [CrossRef]
35. Zhang, Z.-W.; Li, Q.; Zhang, Y.-H.; Wang, H.-L. Simulation and experimental study of effect of vortex finder structural parameters on cyclone separator performance. *Sep. Purif. Technol.* **2022**, *286*, 120394. [CrossRef]
36. Cortés, C.; Gil, A. Modeling the gas and particle flow inside cyclone separators. *Prog. Energy Combust. Sci.* **2007**, *33*, 409–452. [CrossRef]
37. Yao, Y.; Huang, W.; Wu, Y.; Zhang, Y.; Zhang, M.; Yang, H.; Lyu, J. Effects of the inlet duct length on the flow field and performance of a cyclone separator with a contracted inlet duct. *Powder Technol.* **2021**, *393*, 12–22. [CrossRef]
38. Noh, S.-Y.; Heo, J.-E.; Woo, S.-H.; Kim, S.-J.; Ock, M.-H.; Kim, Y.-J.; Yook, S.-J. Performance improvement of a cyclone separator using multiple subsidiary cyclones. *Powder Technol.* **2018**, *338*, 145–152. [CrossRef]